journal

J. Am. Ceram. Soc., **81** [11] 2917–26 (1998)

Direct Measurement and Interpretation of Electrostatic Potentials at 24° [001] Tilt Boundaries in Undoped and Niobium-Doped Strontium Titanate Bicrystals

Zhigang Mao,† Rafal E. Dunin-Borkowski,‡ Christopher B. Boothroyd, and Kevin M. Knowles*

Department of Materials Science and Metallurgy, University of Cambridge, Cambridge CB2 3QZ, United Kingdom

Phase contrast techniques in the transmission electron microscope are used to measure electrostatic potentials at 24° [001] tilt boundaries in nominally undoped and Nb-doped $SrTiO_3$ bicrystals. All of the boundaries are found to have lower scattering potentials than the surrounding bulk crystal. Origins for the measured changes in potential are investigated through the application of high-resolution transmission electron microscopy, diffuse dark-field imaging, energy dispersive X-ray spectroscopy, and parallel electron energy loss spectroscopy. Significantly, we show that space charge is not the dominant contribution to the potential because the magnitudes of the potentials seen cannot be explained on the basis of ionic space charge theory alone.

I. Introduction

MANY of the properties of electronic ceramics are controlled by segregation, nonstoichiometry, and space charge at grain boundaries. These effects are particularly important in donor-doped ZnO varistors, positive temperature coefficient of resistance ceramics such as donor-doped $BaTiO_3$, and internal boundary layer capacitors (IBLCs) in *n*-type semiconducting ceramics.[1–3] The depletion, or space charge, layers that are formed at the grain boundaries in such materials can be described as back-to-back double Schottky barriers, as the negatively charged boundary states are typically compensated by wider positively charged regions in the adjacent bulk material. Impedance analysis has been used to confirm the presence of highly resistive grain boundary layers in both $SrTiO_3$ and $BaTiO_3$ perovskite ceramics and in $SrTiO_3$ internal boundary layer capacitors (IBLCs).[4–6]

Since the space charge layers present at such grain boundaries are necessarily associated with local changes in electrostatic potential, it should be possible to quantify the charge density distributions of the boundary states and the free carriers in the transmission electron microscope (TEM) using phase contrast techniques such as electron holography[7] or Fresnel contrast analysis,[8,9] both of which are sensitive to local changes in specimen potential. Indeed, Ravikumar *et al.*[10] applied electron holography to the characterization of boundaries in acceptor (Mn)-doped $SrTiO_3$ and interpreted their results directly in terms of a dominant contribution to the contrast from ~6 nm wide space charge layers at each boundary. Mao and Knowles[6] used Fresnel contrast analysis and AC impedance techniques to characterize grain boundaries in $SrTiO_3$ IBLCs and demonstrated clear differences in the magnitude of the boundary Fresnel contrast between niobium-doped $SrTiO_3$ semiconducting ceramics and $SrTiO_3$ IBLCs donor-doped with niobium and acceptor-doped with lithium.

Our aim here is to apply Fresnel contrast analysis to the direct measurement of interfacial potentials at boundaries in both undoped and doped $SrTiO_3$, and to assess whether these can indeed be explained by a dominant contribution to the potential associated with the presence of space charge, as has been suggested by other authors. Origins for the measured changes in potential will be investigated through the application of high-resolution transmission electron microscopy (HRTEM), diffuse dark-field imaging, parallel electron energy loss spectroscopy (parallel EELS), and energy dispersive X-ray spectroscopy (EDX). In order to avoid the need for consistent and representative results from a large number of boundaries in a polycrystalline ceramic, we have chosen to examine 24° [001] tilt boundaries in undoped and Nb-doped $SrTiO_3$ tilt bicrystals. These should have boundary structures that are well-defined and similar for both the undoped and the doped specimens.

II. Experimental Details

Melt-grown 24° [001] symmetrical tilt $SrTiO_3$ bicrystals were obtained in 10 mm × 10 mm × 0.5 mm blocks from the Shinkosha Co. Ltd., Tokyo, Japan. Nominal doping levels for the samples, which were either undoped or doped with Nb, were 0, 0.05, and 0.5 wt% Nb for the three samples M1, M2, and M3, respectively. These doping levels correspond to donor concentrations, N_d, of 0, 1.6×10^{25}, and 1.6×10^{26} m^{-3}, respectively, in comparison with the host Sr^{2+} and Ti^{4+} ion concentrations of 1.7×10^{28} m^{-3} and the O^{2-} ion concentration of 5.0×10^{28} m^{-3}. Samples were prepared for transmission electron microscopy using standard ion beam milling procedures.[11] The boundaries were examined edge-on in the orientation shown schematically in Fig. 1 using Fresnel contrast analysis as well as HRTEM, diffuse dark-field imaging, EDX, and EELS. The electrical resistivities of the Nb-doped specimens were determined at room temperature, at an oxygen partial pressure P_{O_2} of 0.21 atm, using a Philips PM2521 automatic multimeter.

III. Experimental Results

(1) Resistivity Measurements

Electrical resistivities, ρ, were measured to be 7.9×10^{-2} Ω·m for M2 and 9.6×10^{-4} Ω·m for M3. On the assumption that, at the donor concentrations examined, donors are compensated by a combination of electrons and strontium vacancies,[12] so that electrons are the excited charge carriers, the mobile electron concentrations, n_e, can be calculated from the formula

T. E. Mitchell—contributing editor

Manuscript No. 191116. Received April 1, 1997; approved February 23, 1998.

Support for R.E.D. was provided by the Engineering and Physical Sciences Research Council, United Kingdom. Support for Z.M. was provided by the Cambridge Commonwealth Trust through the award of a Schlumberger Cambridge Scholarship.

*Member, American Ceramic Society.

†Present address: Department of Chemical Engineering and Materials Science, University of Minnesota, Minneapolis, Minnesota 55455-0132.

‡Present address: Center for Solid State Science, Arizona State University, Tempe, Arizona 85287-1704.

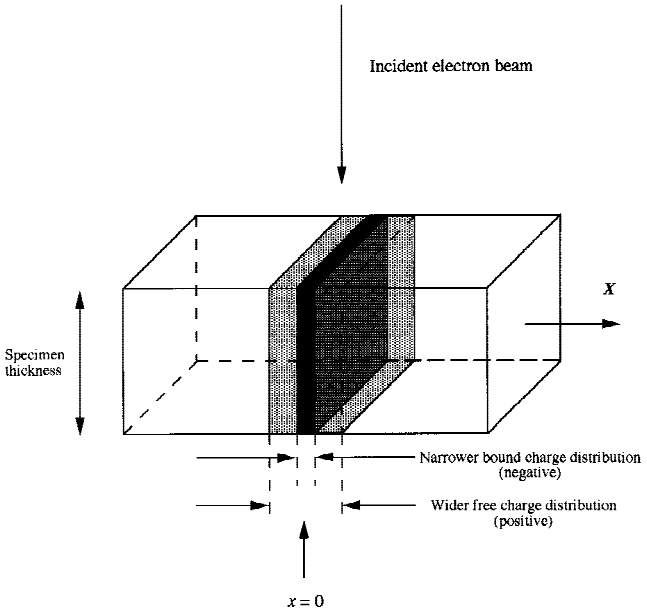

Fig. 1. Schematic diagram showing the orientation of the tilt boundaries and the associated space charge regions with respect to the incident electron beam within the cross-sectional TEM specimens examined.

$$n_e = \frac{1}{e\mu\rho} \tag{1}$$

where e is the electronic charge and μ is the electron mobility, which is reported to be 6×10^{-4} $m^2 \cdot V^{-1} \cdot s^{-1}$ at room temperature.[13] The resulting electron concentrations of $\sim 1 \times 10^{23}$ and $\sim 1 \times 10^{25}$ m^{-3} for M2 and M3, respectively, are significantly less than the corresponding donor concentrations. This is consistent with strontium vacancies being the dominant compensators in the doped materials, given the equality

$$N_d = n_e + 2[V''_{Sr}] \tag{2}$$

where $[V''_{Sr}]$ is the strontium vacancy concentration, as a special case of the generalized neutrality condition for a perovskite crystal.[14]

(2) HRTEM and Diffuse Dark-Field Imaging

HRTEM images were obtained at 200 kV using a JEOL 4000EX-II microscope ($C_s = 0.9$ mm). Clear continuation of lattice fringes was observed across the tilt boundaries in each specimen, and no difference between the undoped and doped specimens could be found. An image of a typical boundary in specimen M1 is shown in Fig. 2, together with a diffraction pattern obtained from the same area. The tilt angle of the bicrystals, as measured from the diffraction pattern, is $24 \pm 0.5°$, which is between the tilt angles for $\Sigma = 13$ [001] (22.62°) and $\Sigma = 85$ [001] (25.06°) symmetrical tilt grain boundaries.

Although each boundary appeared from HRTEM to be free from amorphous material, by virtue of the lattice fringes extending up to the boundary, the danger of such an inference is illustrated by the diffuse dark-field images from specimens M1 and M2 shown in Fig. 3. These were obtained at 200 kV using a JEOL 2000FX microscope with the objective aperture placed well away from any diffraction spots at an effective interplanar spacing of ~0.4 nm. The bright contrast visible at each boundary is strongly indicative of the presence of a layer of some amorphous or disordered material. Qualitatively, the doped specimen, M2, shows brighter contrast at the position of the layer. The contrast from M3 was even more marked at the boundary. The observed contrast in both micrographs in Fig. 3 is not consistent with preferential etching of the boundary and subsequent sputter deposition or damage in these regions, both because the contrast increases with specimen thickness and because no preferential etching of the boundaries was observed at the specimen edge in any of the specimens examined. Thus, although the boundaries in each of the three specimens show continuation of lattice fringes to the boundary, some amorphous material is almost certainly present, appearing to increase with Nb concentration.

(3) Microanalysis

EELS and EDX analyses were carried out at 100 kV in a VG HB501 scanning transmission electron microscope (STEM) using a probe size of 1–2 nm in order to obtain information about changes in the concentration and coordination of the constituent elements across the boundaries. Parallel EELS was used primarily for examining changes in Ti and O coordination and EDX primarily to examine changes in Nb concentration. The energy resolution of the EELS system had been measured previously as 0.4 eV.

Representative EELS spectra obtained from both the bulk $SrTiO_3$ and the boundary in specimen M1 are shown in Fig. 4. The lack of a detectable change in the Ti $L_{2,3}$ edge between the two regions is consistent with results obtained from a similar undoped specimen by McGibbon *et al.*,[15] who were able to conclude that the octahedral Ti–O coordination is maintained across the boundary. However, McGibbon *et al.*[15] also noted a

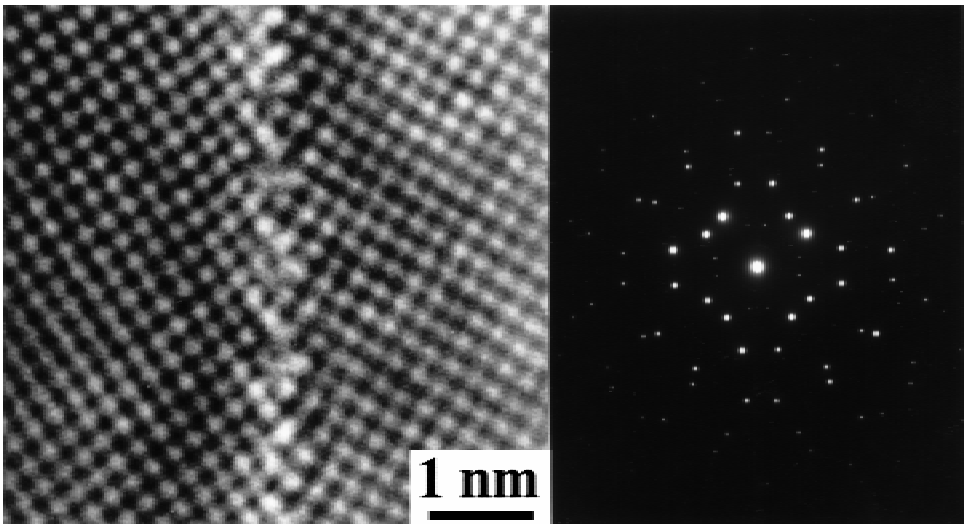

Fig. 2. A typical region of an HREM image and the corresponding electron diffraction pattern with the incident electron beam down the common [001] direction. This was obtained from the boundary in specimen M1.

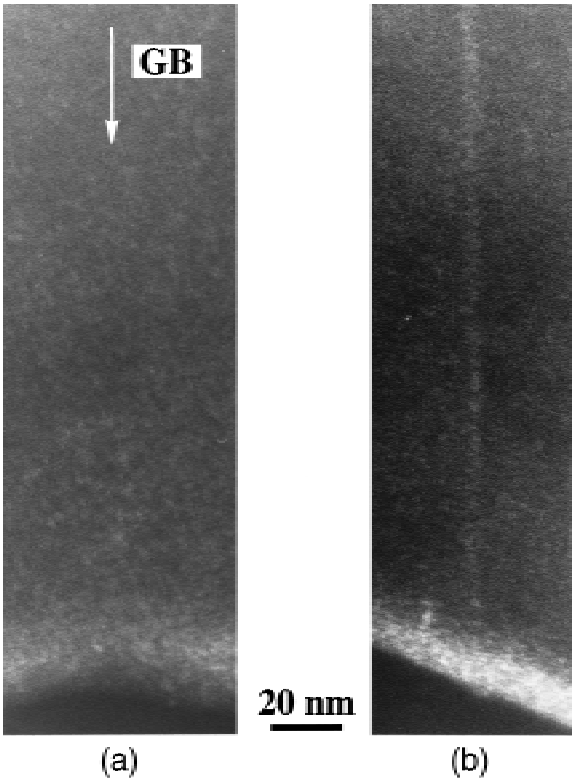

Fig. 3. Centered diffuse dark-field images obtained from (a) M1 and (b) M2, with the objective aperture placed away from any diffraction spots at an effective interplanar spacing of approximately 0.4 nm.

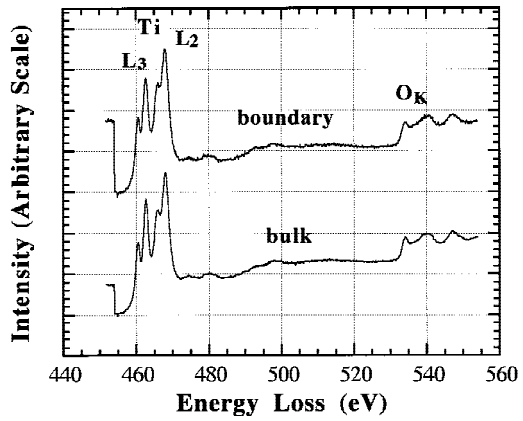

Fig. 4. Representative EELS spectra from boundary and bulk regions in M1.

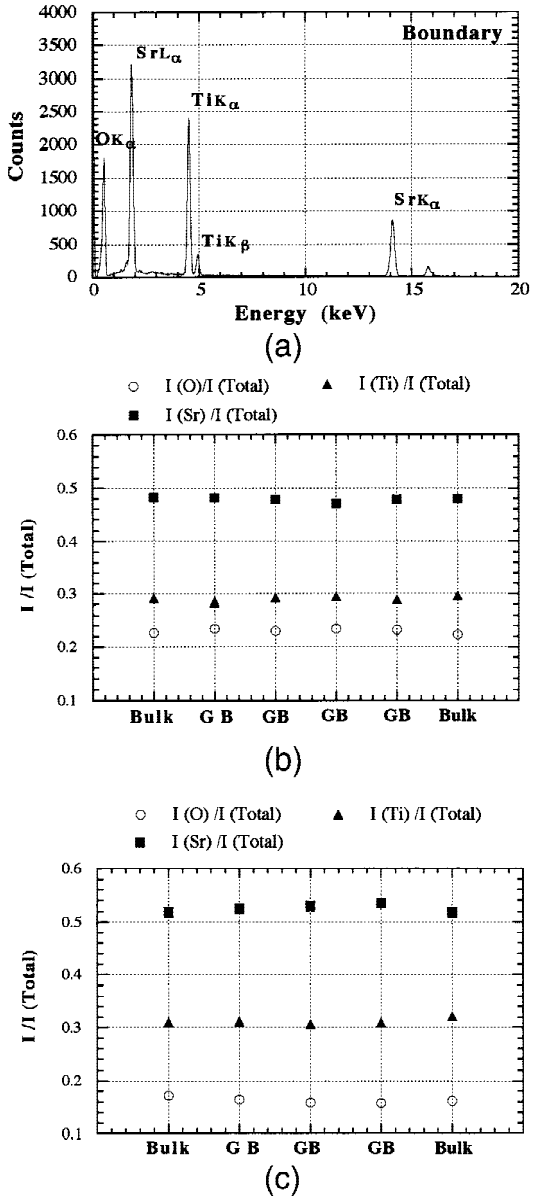

Fig. 5. (a) Typical EDX spectrum obtained from specimen M3. Nb L_α (2.166 kV) and L_β (2.257 kV) peaks were not detected. (b) and (c) show ratios of the areas under the peaks corresponding to O, Sr, and Ti divided by the total area under the peaks for specimens M1 and M3, respectively, for both bulk and grain boundary (GB) regions.

change in the fine structure of the O *K* edge at the boundary and attributed this to distortions of the Ti–O bonds in the grain boundary region. Such a change in the O *K* edge between the boundary and the bulk was not observed in our data, possibly as a result of the poorer energy resolution of our system as compared with that of McGibbon *et al.*[15] Spectra obtained from specimens M2 and M3 were similar to those in Fig. 4, and also did not show any differences between the bulk $SrTiO_3$ and the boundaries.

EDX spectra were obtained from both bulk and boundary regions in specimens M1 and M3, with negligible specimen drift occurring during acquisition of each spectrum. A representative spectrum from the boundary in specimen M3 is shown in Fig. 5(a). Nb, with its L_α and L_β peaks at energies of 2.166 and 2.257 kV, respectively, could not be detected in spectra obtained from any of the specimens. Ratios of the area beneath the peak corresponding to each element divided by the area under all of the peaks added together are shown in Figs. 5(b) and (c) for specimens M1 and M3, respectively. There are no convincing differences between the ratios for the bulk material and the boundary in either specimen, although systematic differences are present between the specimens because of the different specimen thicknesses examined. The lack of detectable Nb segregation is in agreement with the results of Chiang and Takagi,[16] as well as with a simple calculation[17] of the misfit energy associated with Nb^{5+} substituting for Ti^{4+}. A full error analysis of the EDX data was carried out in order to determine the maximum possible difference between the concentration of each element in the bulk material and at the boundary in each specimen. The results are shown in Table I. The procedure used to calculate the errors quoted in this table is described in the Appendix. If the concentration of each element were to change uniformly across a layer of width $d \sim 0.5$ nm, and if the probe diameter, $2r$, is taken to be 3 nm (allowing for slight specimen drift), over which collection of

Table I. Intensity Ratios Obtained from Areas Beneath Peaks in EDX Traces†

Sample		I_O/I_{total}	I_{Sr}/I_{total}	I_{Ti}/I_{total}	I_{Nb}/I_{total}
M1	Bulk	0.2269 ± 0.0021	0.4822 ± 0.0021	0.2910 ± 0.0021	
	B1	0.2346 ± 0.0021	0.4813 ± 0.0021	0.2841 ± 0.0021	
	B2	0.2302 ± 0.0021	0.4781 ± 0.0021	0.2917 ± 0.0021	
	B3	0.2349 ± 0.0021	0.4708 ± 0.0021	0.2943 ± 0.0021	
	B4	0.2331 ± 0.0021	0.4783 ± 0.0021	0.2886 ± 0.0021	
	Bulk	0.2238 ± 0.0021	0.4801 ± 0.0021	0.2961 ± 0.0021	
M3	Bulk	0.1718 ± 0.0014	0.5182 ± 0.0018	0.3100 ± 0.0017	0 ± 0.0005
	B1	0.1642 ± 0.0014	0.5245 ± 0.0018	0.3113 ± 0.0017	0 ± 0.0005
	B2	0.1581 ± 0.0014	0.5296 ± 0.0018	0.3065 ± 0.0017	0 ± 0.0005
	B3	0.1573 ± 0.0014	0.5340 ± 0.0018	0.3087 ± 0.0017	0 ± 0.0005
	Bulk	0.1612 ± 0.0014	0.5184 ± 0.0018	0.3204 ± 0.0017	0 ± 0.0005

†The number of counts recorded for each peak was greater than 10 000. B1, B2, B3, and B4 denote spectra obtained from the boundaries. $I_{Sr} = I_{SrL_\alpha} + I_{SrK_\alpha}$ and $I_{Ti} = I_{TiK_\alpha} + I_{TiK_\beta}$. The procedures used to calculate the errors quoted in this table are described in the Appendix.

X-rays is assumed to be uniformly efficient, then to a good approximation the contribution of the boundary will be a fraction $2d/\pi r$ of the total count for a given element. Thus, the errors quoted in Table I correspond to upper limits for the changes in composition between the bulk material and the boundary in each specimen of 2 at.% for each of O, Sr, and Ti, and 1 at.% for Nb.

(4) Fresnel Contrast Analysis

The TEM-based technique of quantitative Fresnel contrast analysis[8,9] involves the matching with computer simulations of a through-focal series of images of an interlayer examined in cross section. To first order, the spacing and the contrast of the Fresnel fringes visible at the layer are sensitive to the width and the magnitude of the change in potential, respectively, while the detailed changes in fringe contrast with defocus can be used to determine the shape of the potential profile. The sensitivity of the experimental Fresnel fringes to the form of the potential generally increases as the experimental beam convergence is decreased. The most serious limitations to the quantitative application of the technique include the presence of contributions to the contrast from inelastic scattering, which is difficult to include in simulations, and the requirement for an accurate value of the specimen thickness of the region analyzed. Accordingly, our data were energy-filtered to remove from the images the electrons that had been inelastically scattered within the specimen, and the specimen thickness was always determined accurately using weak-beam dark-field thickness fringes.

Energy-filtered Fresnel series of the boundary in each specimen were obtained at 397 kV in a JEOL 4000FX microscope (C_s = 2.0 mm, C_c = 1.4 mm) equipped with a postcolumn Gatan imaging filter (GIF). Care was taken to ensure that the boundaries were vertical with respect to the incident electron beam, and that diffraction contrast from the bulk regions of crystal was low. An energy-selecting slit of width 10 eV, centered on the zero-loss peak, was used to energy-filter the data. The acquisition time for each image was approximately 5 s. The nominal microscope magnification was 4000, with the GIF providing a further increase in magnification of approximately 20. The images were captured onto a 512 × 512 pixel CCD array at a sampling density relative to the specimen of approximately 0.3 nm per pixel, and the point spread function of the CCD was deconvoluted from each image. The defocus step size between the images in each series was found to be 809 nm from power spectra obtained from regions of amorphous carbon at the specimen edge close to the area of interest.

Two of the images obtained from specimen M3 are shown in Fig. 6. These correspond to approximately seven steps of 809 nm underfocus and overfocus, respectively, with respect to Gaussian focus. The region chosen for subsequent detailed Fresnel fringe analysis is shown boxed in both micrographs. The objective aperture used for these micrographs had a semi-angle of 3.8 mrad. The large number of Fresnel fringes visible in Figs. 6(a) and (b) arises from the low value of the experimental beam convergence used, which was measured to be 0.17 mrad for these images. This enables the data to be fitted to image simulations to high accuracy.

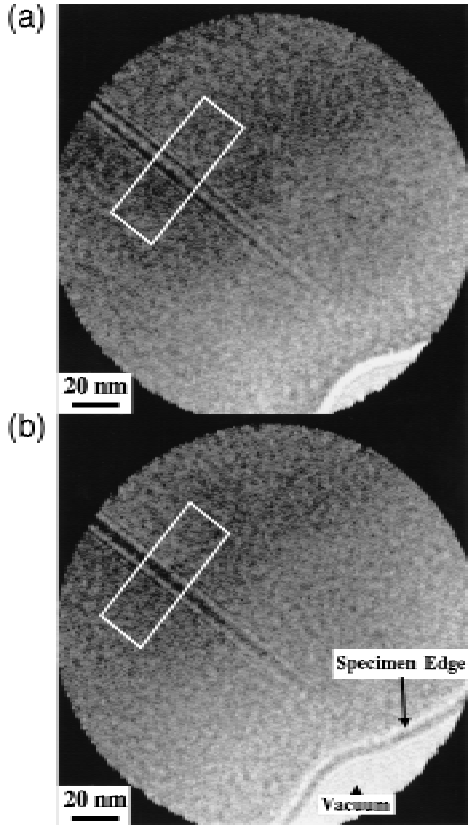

Fig. 6. Fresnel contrast images of the boundary in specimen M3, taken at approximately 7 steps of 809 nm underfocus (a) and overfocus (b).

Montages of the selected regions for specimens M1, M2, and M3, which were taken at measured specimen thicknesses of 42, 37, and 32 nm, objective aperture semi-angles of 3.8, 9.6, and 3.8 mrad, and measured beam convergences of 0.12, 0.21, and 0.17 mrad, respectively, are shown as a function of defocus in Fig. 7. Significantly, the contrast from the undoped specimen is much fainter than that from the two doped specimens, indicating that the presence of niobium must be affecting the scattering potentials of the boundaries in the doped specimens. The boundaries in all three specimens exhibit a bright central fringe underfocus and a dark central fringe overfocus. If by convention the potential within the specimen is taken to be positive, so that there are maxima at the atomic positions, the imaging

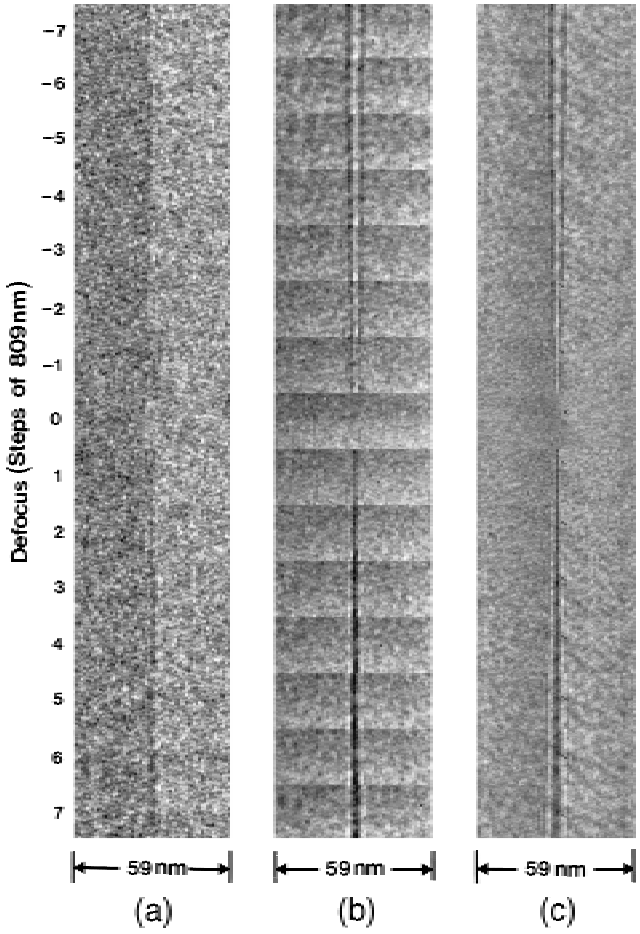

Fig. 7. Montages showing the regions chosen for analysis as a function of defocus in (a) M1, (b) M2, and (c) M3, respectively.

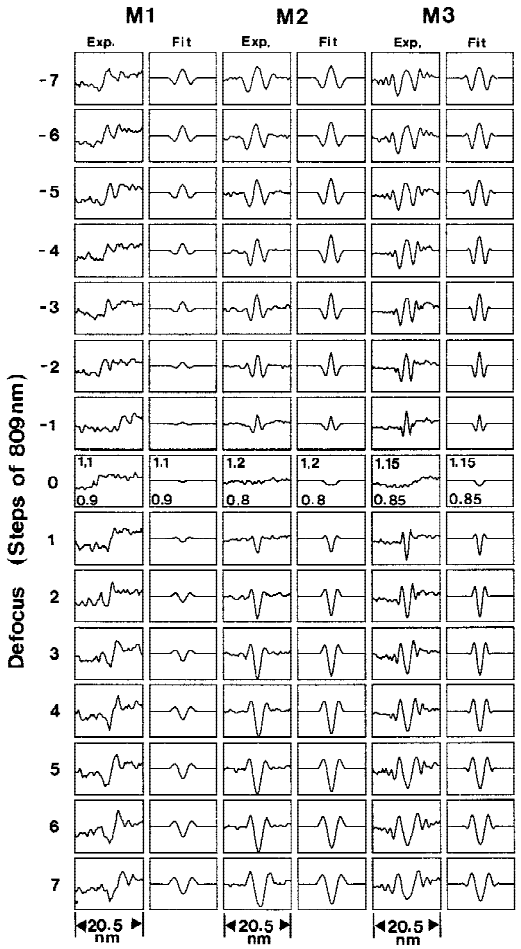

Fig. 8. One-dimensional projected Fresnel fringe profiles corresponding to the montages shown in Fig. 7, together with the best-fitting profiles.

behavior of the boundary relative to the bulk is characteristic of a *lower*, less positive, scattering potential at the boundary relative to the bulk material.[8,9]

A number of factors contribute to the measured change in potential at an interface, as we discuss in Section IV. However, it is instructive at this stage of the analysis to specify what contrast we would expect if the contrast were to be dominated by the presence of a depletion, or space charge, layer. If space charge effects dominate the Fresnel contrast that we observe, then the presence of a lower scattering potential at the boundary would indicate that the charge localized at the boundary is *negative* and the surrounding charge distribution *positive*. This would be the case for an *n–p–n* junction, in which the *p*-type layer is localized at the boundary and is bounded on both sides by *n*-type material and where the depletion layers are then responsible for the sign of the charge distributions. (The sign of the change in potential can be understood by analogy with an isolated atom, which corresponds to a localized region of positive charge and a wider distribution of negative charge, and for which the spatially averaged potential is positive.[18])

The intensity in the experimental images shown in Fig. 7 was projected parallel to the direction of the boundaries. The resultant one-dimensional line profiles of intensity against distance are shown in Fig. 8, together with best-fitting simulated profiles. These were obtained using multislice calculations[8,9] incorporating a slice thickness of 0.5 nm parallel to the electron beam and a sampling density of 0.050 nm per pixel. Potential profiles were included in the multislice calculations in the form of one-dimensional mean potential or ''continuum'' models.[8,9] Only after best-fitting potential profiles had been obtained in this manner was interpretation in terms of changes in composition, density, and space charge attempted. A Simplex algorithm[19] was used to vary the width, the depth, and the shape of the potential wells in the simulations iteratively, at the same time as refining the values of the experimental beam convergence and the starting defocus value for each series. The fitting procedure will be described in detail elsewhere,[20] but briefly a goodness-of-fit criterion (defined as the mean value of the squared difference between the experimental and simulated Fresnel fringes) was minimized by varying the well shape and microscope parameters using a multidimensional minimization algorithm based on a geometrical figure linking vertices describing the parameters being varied. Several starting configurations of well width, shape, and depth were used in the calculations in order to ensure that identical fitted potential profiles corresponding to global minima were obtained each time.

The potential profile was always included in the simulations in the form of a difference of two exponentially decaying functions, so that if the dominant contribution to the potential were indeed associated with the effects of space charge, the potential could be interpreted directly in terms of the widths and the charge densities of the narrower and the wider charge density distribution at the position of the layer. (Both segregant and free charge profiles at surfaces and interfaces are usually modeled as exponential distributions; see Section IV(4)(C), for example). The imaginary part of the scattering potential was also fitted, in the form of a constant fraction of the real part of the potential. To first order, this describes the variation in the intensity scattered outside the objective aperture across the position of the boundary, a higher value of the imaginary part of the scattering potential indicating greater scattering to large angles. The best-fitting potential profiles to the experimental data are shown in Figs. 9(a) and (b). The corresponding pa-

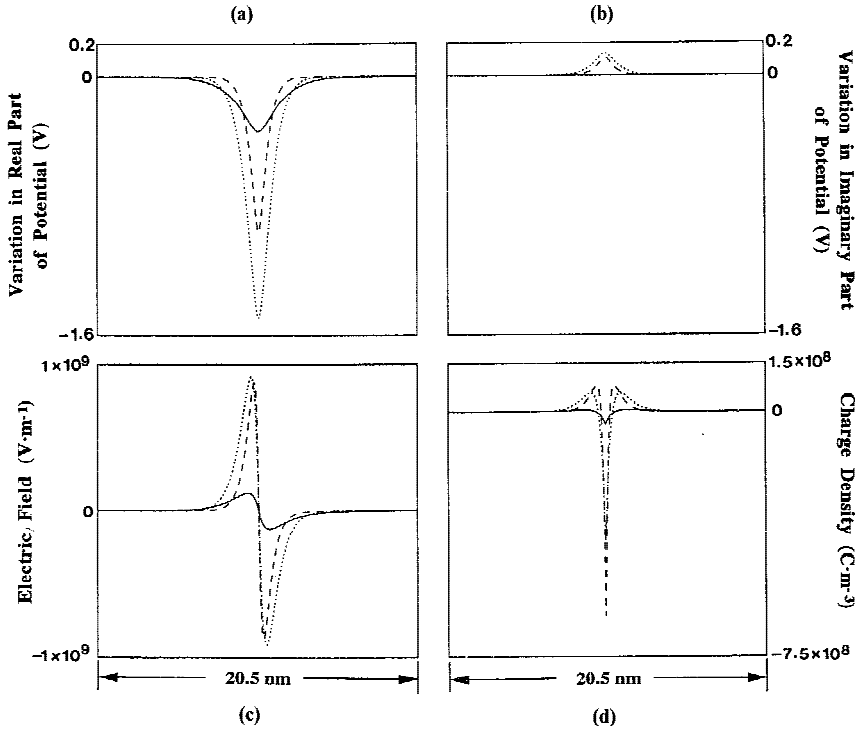

Fig. 9. Best-fitting potential profiles across the boundaries in the three specimens examined. In each diagram, the solid, dotted, and dashed lines correspond to specimens M1, M2, and M3, respectively. The variation in the real and imaginary parts of the potential are shown in (a) and (b). The electric field and charge density profiles obtained by applying Poisson's equation to the potential profiles in (a) are shown in (c) and (d).

rameters describing the well widths and depths (denoted ΔV) are given in Table II.

IV. Analysis of the Potential Profiles

Several inferences can be drawn immediately from the shapes of the profiles in Fig. 9 and the values of the fitted parameters in Table II:

(i) It is particularly interesting to observe that, while the well width decreases with increasing Nb concentration, the well depth does not change monotonically. While the origin of the variation in potential in each specimen is not known at this stage of the analysis, this decrease in well width with increasing dopant concentration is of significance. It will be shown below that most models for space charge layers predict that the width of the wider free carrier distribution should indeed decrease as the electrically active concentration at the boundary increases. The magnitude of ΔV also depends sensitively on the spatial extent of the free carriers for a given value of the electrically active concentration.[18]

(ii) The form of the imaginary part of the potential (describing scattering to large angles) is also significant. It can be seen that the boundary in the undoped specimen, M1, scatters negligibly outside the objective aperture in comparison with the surrounding bulk $SrTiO_3$. This is in contrast to the marked increase in high-angle scattering at the boundaries in the doped specimens, M2 and M3. The presence of niobium is therefore associated with a change in the angular scattering behavior at the boundaries, despite the fact that niobium is conventionally considered to be a bulk dopant! It is particularly unusual that the real and imaginary parts of the fitted potential are opposite in sign—a decrease in the real part of the potential is generally associated with *less* scattering to high angles.[8,9] This point will be discussed further below.

Table II. Parameters Describing the Best-Fitting Potential Profiles

	ΔV (V)	fwhm (nm)†	Absorption (fraction)
M1	−0.34	3.37	−0.002
M2	−1.49	2.02	−0.090
M3	−0.96	1.35	−0.115

†Full width at half-maximum.

There are various possible origins for the change in the scattering potential at an interface within a material, and several of these may be present at once. We will therefore assess each one of a number of possibilities systematically, in order to assess whether one possibility alone could account for the results or whether a suitable combination is required. We will concentrate on the effect of changes in composition, density, and space charge on the scattering potential. However, we will not consider the effect of dipole layers on the specimen surfaces, which can affect the mean value of the scattering potential in a material, are sensitive to the presence of adsorbed layers,[21] and may change across the specimen surfaces in the vicinity of the boundaries. The magnitude of this contribution requires further investigation. We will also neglect the presence of leakage fields[22] outside the specimen, as their effect on Fresnel contrast has been shown to be negligible for the specimen thicknesses examined here.[23]

(1) Changes in Scattering Factor

The effect of variations in composition and density on the scattering potential, V_0, can be expressed using the equation[24]

$$V_0 = \frac{h^2}{2\pi m_e e \Omega} \sum_{\substack{\text{atoms in} \\ \text{the unit cell}}} f_{el}(0) \tag{3}$$

where Ω is the unit cell volume, h is Planck's constant, m_e is the electronic rest mass, and $f_{el}(0)$ is the electron scattering factor at zero scattering angle for each atom or ion in the unit cell. Since the bonding character between atoms affects $f_{el}(0)$ strongly but is difficult to include in computer calculations of V_0 for all but the simplest materials,[21] we will consider here the extreme limits of materials that are either fully neutral or fully ionic. This approach is justified by the fact that we were unable to detect any differences in bonding character between the bulk

$SrTiO_3$ and the boundaries using EELS. Values of $f_{el}(0)$ for neutral and fully ionic Sr, Ti, O, and Nb calculated by Rez *et al.*[25] are given in Table III. These will now be used to assess the effect of a change in composition on the potential, given the restriction on the allowed change in the concentration of each species imposed by the EDX results.

The calculated values of V_0 for fully neutral and fully ionic $SrTiO_3$ with a unit cell of side 0.3905 nm are 22.3 and 15.1 V, respectively. A simple increase in ionic character at the grain boundary relative to the bulk material without a change in composition would thus provide a decrease in scattering potential. However, it is difficult to imagine that this is the sole origin of the variation in potential observed in the experimental data because bulk $SrTiO_3$ is known to be almost fully ionic.[12]

Nb is predicted to substitute only for Ti as a result of both the valencies and the ionic radii of the atomic species.[12] It is therefore interesting to note that qualitatively an increase in the concentration of Nb substituting for Ti with a corresponding increase in the concentration of Sr vacancies to maintain charge neutrality would lower the scattering potential in the doped specimens, assuming that at sufficiently low Nb concentrations the lattice parameter of the $SrTiO_3$ is unchanged. Preliminary calculations[26] using the thermal diffuse scattering routines derived by Weickenmeier and Kohl[27] indicate that this would also explain the increase in scattering outside the objective aperture required to reproduce the sense of the absorption contrast measured for the two doped specimens.

However, quantitatively, the changes in the total Nb concentration at the center of the layer that would be required to reproduce the experimental values of ΔV are significantly higher than the maximum increase of 1 at.% allowed from the EDX data. Specifically, if there is $2x$ at.% Nb substituting for Ti and an increase of x at.% Sr vacancies to maintain charge neutrality, then the change in scattering potential ΔV_0 would be given by the formula

$$\Delta V_0 = 0.807\{2x\,(f_{Nb} - f_{Ti}) - xf_{Sr}\} \text{ volts} \quad (4)$$

and so for $2x = 0.01$, in line with the microanalysis data, $\Delta V_0 = -0.009$ V for fully ionic material and -0.037 V for fully neutral material. Therefore, this cannot be the sole origin of the observed changes in potential in the doped specimens.

(2) Changes in Density

The changes in density alone without a change in composition that would be required to reproduce the magnitudes of the best-fitting potential profiles, such as would be associated with the presence of an amorphous layer or an increase in disorder at the boundaries, are shown in Table IV. Given that the differences between the scattering potentials of fully crystalline and fully amorphous ceramics of identical compositions are usually of the order of 10%,[28] if a change in density alone were responsible for the measured potential profiles, the boundaries would have a density corresponding to a material that is almost completely amorphous with widths of the order of the full widths at half-maximum quoted in Table II. However, the presence of such amorphous interlayers is at variance with our high-resolution images.

(3) Changes in Both Scattering Factor and Density

From the discussion in the preceding two sections (IV(1) and IV(2)), it is apparent that while no single contribution can account for the experimentally measured values of ΔV, a suitable combination of changes in scattering factor and density, such as a local increase in Nb concentration together with a degree of disorder providing a decrease in density, would do so. We will return to this point later, but for now turn to an assessment of the possible contribution to the potential from space charge.

Table III. Electron Scattering Factors (Å) at Zero Scattering Angle†

O	1.98	O^{2-}	4.10
Sr	13.00	Sr^{2+}	4.64
Ti	8.73	Ti^{4+}	1.84
Nb	10.70	Nb^{5+}	3.08

†From Ref. 25.

Table IV. Percentage Decrease in Density without a Change in Composition Required to Explain the Experimental Changes in Boundary Potential for Both Neutral and Ionic Scattering Factors

Sample	Density decrease (%)	
	Neutral	Ionic
M1	1.5	2.3
M2	6.7	9.9
M3	4.3	6.4

(4) Space Charge

In order to obtain an understanding of the parameters that are required to describe the space charge layers that would reproduce the experimentally measured potential profiles, we will consider initially a simple model comprising one positive and one negative exponentially decaying charge density distribution at the boundary in each specimen, before examining models based on Schottky barriers and Boltzmann statistics. The static relative permittivity of $SrTiO_3$, ε_r, will be taken to be 300 for all of the calculations presented below.[12] For reference, the electric field and the charge density that are obtained simply by applying Poisson's equation to the experimentally measured potential profiles are shown in Figs. 9(c) and (d).

(A) One Positive and One Negative Exponentially Decaying Charge Density Distribution: When fitting the experimental Fresnel fringes to simulations, a good fit to the experimental data was provided by a potential profile that took the form of a difference between two exponential functions. This choice immediately provides an estimate for both the widths and the magnitudes of the positive and negative charge density distributions that would provide a fit to the experimental data. We will use the symbols d_b for the full width at half-maximum (fwhm) of the narrower (negative) charge density profile, d_f for the fwhm of the wider (positive) charge distribution, and N_{2D} for the electrically active concentration of each of these expressed as if all of the charge were concentrated into a single sheet.[20] Values of d_b, d_f, and N_{2D} that fit the experimental data, on the assumption that the measured potential profiles can be accounted for *solely* by the contribution from the space charge potential, are given in Table V. The values of N_{2D} that would be required are clearly very large, at between 1.0×10^{19} and 2.4×10^{20} atoms·m^{-2}, as a direct result of the high relative permittivity of $SrTiO_3$. For comparison, a unit cell of $SrTiO_3$ projected onto the side of the cubic unit cell is equivalent to a density of 1.9×10^{19} atoms·m^{-2}.

(B) Schottky Barrier: An interfacial space charge layer can be modeled as a back-to-back double Schottky barrier.[29] The simple theory for this assumes that the electronic boundary states are restricted to the interface plane, that the bulk material is homogeneously doped, that the dopant shows no change in valency as a function of distance from the boundary plane, and

Table V. Values of d_b, d_f, and N_{2D} Fitted to the Experimental Boundary Potential Profiles

Sample	d_b (nm)†	d_f (nm)‡	N_{2D} (m^{-2})§
M1	0.03	2.25	1.03×10^{19}
M2	0.03	0.98	2.40×10^{20}
M3	0.01	0.87	8.16×10^{19}

†Full width at half-maximum (fwhm) of the narrower (negative) charge density profile. ‡fwhm of the wider (positive) charge distribution. §Electrically active concentration of each of these expressed as if all of the charge were concentrated into a single sheet.

that the depletion of the free carriers has a box-type profile. The height of the potential barrier across the boundary is then given by

$$\phi = \frac{ez\,N_d W^2}{2\varepsilon_0 \varepsilon_r} \tag{5}$$

where N_d is the donor concentration, ε_0 is the permittivity of free space, ε_r is the static relative permittivity, z is the effective charge of the donors, and W is the width of the depletion layer on one side of the boundary. The Debye length, L_D, can be used as a measure of W.[14,29] For the situation we have here, where the grains are *n*-type and the boundary is *p*-type, L_D is given by the expression

$$L_D = \left(\frac{\varepsilon_0 \varepsilon_r k_B T}{e^2 z^2 N_d}\right)^{1/2} \tag{6}$$

where k_B is Boltzmann's constant and T is the absolute temperature. Values of $2L_D$ and ϕ for a total back-to-back depletion layer width equal to $2L_D$ for M2 and M3 calculated from the above equations for temperatures of 300 and 1600 K assuming a value for z of +1 are given in Table VI. While the sense of the change in ϕ is correct, the magnitudes predicted are much lower than the observed values, and the widths of the depletion regions, W, over which any changes in scattering factor would have to occur to make ϕ the same as the observed values are also too large, as a consideration of Eqs. (5) and (6) shows. Furthermore, even if it assumed that the specimens are not in equilibrium at 300 K but are instead representative of specimens equilibrated at higher temperatures, e.g., 1600 K because of the cooling history of the bicrystal specimens (see, for example, discussion on this topic elsewhere),[30] the data cannot be manipulated to explain our observations. This model will therefore not be considered further.

(C) The Approach of Kliewer and Koehler:[31] In this model, the boundary is assumed to act as a perfect source and sink for ionic defects that are dilute everywhere, and the concentration profile of each species is described using Boltzmann statistics.[31,32] Using the notation of Kröger and Vink,[33] intrinsic defects in the form of O, Sr, and Ti vacancies in pure $SrTiO_3$ are denoted by the symbols $V_O^{\cdot\cdot}$, V_{Sr}'', and V_{Ti}'''', respectively. The height of the potential barrier, ϕ, is obtained using a statistical mechanics approach. This has been applied to problems similar to that considered here by both Desu and Payne[15] and Chiang and Takagi,[17] although unlike in the present work these authors did not measure the experimental changes in potential at their boundaries directly. Following the methodology of these authors, if ΔG_{Sr}, ΔG_{Ti}, and ΔG_O are the free energies of formation of Sr, Ti, and O vacancies, respectively, the height of the potential barrier, $\phi(\infty)$, for differing limiting cases in pure $SrTiO_3$ is given by the expressions

$$e\phi(\infty) = \frac{1}{4}(\Delta G_{Sr} - \Delta G_O + k_B T \ln 3) \qquad (\Delta G_{Ti} >> \Delta G_{Sr}, \Delta G_O) \tag{7}$$

$$e\phi(\infty) = \frac{1}{6}\left(\Delta G_{Ti} - \Delta G_O + k_B T \ln \frac{3}{2}\right) \qquad (\Delta G_{Sr} >> \Delta G_{Ti}, \Delta G_O) \tag{8}$$

Table VI. Values of Twice the Debye Length ($2L_D$) and Potential Barrier Height (ϕ) for the Depletion Layer Width Equal to the Debye Length, Obtained Using the Schottky Potential Model for T = 300 and 1600 K

	300 K		1600 K	
Sample	$2L_D$ (nm)	ϕ (V)	$2L_D$ (nm)	ϕ (V)
M2	10.3	−0.013	24	−0.069
M3	3.3	−0.013	7.6	−0.069

There is disagreement in the literature on the magnitude of the defect formation energies ΔG_{Sr}, ΔG_{Ti}, and ΔG_O (see for example, Refs. 30 and 34), but the limiting cases in these equations provide useful guides as to whether our experimental data can be rationalized in terms of a dominant contribution to the potential observed from space charge.

In donor-doped $SrTiO_3$, as is the case for specimens M2 and M3, the donors are compensated by both electrons and Sr vacancies with vacancy compensation preferred at high oxygen pressures during growth.[35] The space charge potential then takes the form[16]

$$e\phi(\infty) = \frac{1}{2}\left(\Delta G_{Sr} + k_B T \ln \frac{[V_{Sr}'']}{N}\right) \tag{9}$$

where the values of $[V_{Sr}'']$ can be obtained from the resistivity measurements given in Section III and N is the number of Sr^{2+} ions per unit volume. Thus, as the concentration of strontium vacancies increases, e.g., from M2 to M3, we would expect that the space charge potential $\phi(\infty)$, which is opposite in sign to ΔV, would increase, contrary to what we observe experimentally, because the magnitude of ΔV decreases going from M2 to M3 (see Table II). Specifically, if $[V_{Sr}'']$ in M3 is 10 times that in M2 (cf., the resistivity measurements in Section III), then $\Delta\phi = \phi(\infty)_{M3} - \phi(\infty)_{M2} = +0.030$ V at 300 K and +0.159 V at 1600 K, rather than the observed −0.53 V.

The width of the space charge layer can be expressed using a generalized Debye length[36]

$$L_D = \left(\frac{\varepsilon_0 \varepsilon_r k_B T}{e^2 \sum_i z_i^2 n_i(\infty)}\right)^{1/2} \tag{10}$$

where z_i is the effective charge of each extrinsic defect and $n_i(\infty)$ the bulk concentration of each extrinsic defect. To a good approximation, $\phi(x)$ will decay exponentially (or faster—see the discusison in Ref. 31) with distance x from the boundary as

$$\phi(x) = \phi(\infty)\left[1 - \exp\left(\frac{-x}{L_D}\right)\right] \tag{11}$$

so that $2L_D$ can be used as a measure of the width of the depletion layer. The concentration of each defect can be written to a good approximation as

$$n_i(x) = n_i(\infty)\exp\left(\frac{-z_i e[\phi(x) - \phi(\infty)]}{k_B T}\right) \tag{12}$$

The effect of the concentration of each segregant or defect on the potential was included in the calculations in the form of both a change in scattering factor using Eq. (3) and a space charge contribution using Eq. (12). In lieu of any values for ΔG_{Sr}, ΔG_{Ti}, and ΔG_O quoted in the literature, values of $\Delta G_{Ba} = 1.0$ eV and $\Delta G_O = 1.4$ eV quoted by Desu and Payne[14] for $BaTiO_3$ were used for ΔG_{Sr}, and ΔG_O, respectively, given the close similarity between the structures of $SrTiO_3$ and $BaTiO_3$. However, we have assumed that the value for ΔG_{Ti} of 0.8 eV quoted by Desu and Payne[14] for $BaTiO_3$ is unrealistically small for $SrTiO_3$ (see, for example, the comment by Chan, Sharma, and Smyth[37] on V_{Ti}'''' being unfavorable and the discussion by Chiang and Takagi[38]) and have used Eq. (8) to provide the height of the potential barrier in pure $SrTiO_3$.

Results of calculations are shown in Table VII for three temperatures—300, 1200, and 1600 K—at which equilibrium might have been achieved. If Eq. (12) is taken to be a suitable representation of the concentration of niobium as a function of distance from the boundary in M2 and M3, then the magnitudes of the potential barrier calculated from Eq. (9) for both M2 and M3 at 300 K would necessitate gross segregation of niobium to the bicrystal boundaries within the Debye length, contrary to what we have observed from EDX. If we take equilibration to occur at a higher temperature, such as 1200 or 1600 K, or vary the values for ΔG_{Sr} and ΔG_O, agreement between the experi-

Table VII. Predictions from the Theory of Kliewer and Koehler[31] for Values of Twice the Debye Length ($2L_D$) and Potential Barrier Height (ϕ) for T = 300, 1200, and 1600 K†

	300 K		1200 K		1600 K	
Sample	$2L_D$ (nm)	ϕ (V)	$2L_D$ (nm)	ϕ (V)	$2L_D$ (nm)	ϕ (V)
M1		0.107		0.128		0.138
M2	6.0	0.401	12.0	0.105	14.0	−0.028
M3	1.9	0.430	3.9	0.220	4.3	0.128

†We have assumed here that ΔG_{Sr} and ΔG_O take values $\Delta G_{Sr} = \Delta G_{Ba} = 1.0$ eV and $\Delta G_O = 1.4$ eV quoted for ΔG_{Ba} and ΔG_O for $BaTiO_3$,[14] because of the close similarity structurally of $SrTiO_3$ and $BaTiO_3$.

mental data in Table II and the theory remains elusive, although a fit can be obviously forced for the potential barrier height for M1 for a suitably high assumed difference between ΔG_{Sr} and ΔG_O. Thus, our conclusion from these calculations is that, while space charge effects at the boundaries can contribute to the Fresnel fringe contrast that we have observed and hence to the potential profiles that we have deduced, they cannot be the sole contribution. This is perhaps not too surprising; Kliewer and Koehler's theory[31] is for an equilibrium segregation situation at a free surface. Here, equilibrium and nonequilibrium segregation are both possible, depending on the detail of the thermal history of the samples prior to examination in the transmission electron microscope,[30,34] and grain boundaries are internal, rather than free, surfaces.

V. Discussion

It is encouraging that the contribution to the specimen potential from space charge might account for a large proportion of the magnitude of the experimentally observed potential profile in the undoped specimen M1. The fact that a further decrease in scattering potential is required to match the potential profiles exactly for this specimen from our calculations in Table VII and that diffuse dark-field images indicate the presence of amorphous or disordered material at the position of the layer would be consistent with this explanation.

The measured potential profiles for the doped specimens are clearly affected strongly by the presence of Nb and are more difficult to understand, particularly in view of the fact that the EDX spectra indicate that the change in Nb concentration between the bulk material and the boundaries must be less than 1 at.%. The depths of the measured potential profiles cannot be accounted for by any individual contribution to the change in potential from those considered, and in particular neither the presence of a space charge layer nor a decrease in density without a change in composition, as suggested by the diffuse dark-field images, can account for the experimental contrast. However, it should be noted that the decrease in the widths of the measured potential profiles with increasing dopant concentration is consistent with an interfacial potential that can be explained at least partly by the effects of space charge, even if they do not dominate the depths of the observed potential wells. Although the EDX spectra also preclude the presence of a sufficient change in the concentration of Nb substituting for Ti that would be required for the potential to be dominated by changes in scattering factor, it is particularly interesting to note that the presence of a small degree of Nb segregation would account for the increased scattering out of the objective aperture observed at the positions of the layers.

The above observations must also be consistent with the continuation of lattice fringe contrast observed across the boundaries. It is thus most likely that the depths and the widths of the potential profiles measured at the boundaries in the doped specimens can be accounted for partly by a space charge potential, partly by the substitution of Nb for Ti, and partly by the presence of amorphous material or an increase in disorder at the boundaries. In order to assess the latter contribution quantitatively, one approach would be to determine the degree to which there is a rigid lattice shift across the boundaries, as compared with models of predicted boundary structures, from a careful extrapolation toward the boundary of lattice fringes obtained from perfect regions of crystal on either side of the layer, using an approach similar to that of Wood *et al.*[39] The results of such an investigation will be presented elsewhere.

VI. Conclusions

The local changes in potential across tilt boundaries in undoped and Nb-doped strontium titanate bicrystals have been measured directly using phase contrast techniques in the TEM. These have been interpreted in detail. Our analysis of the potential profiles shows that space charge cannot be the sole origin of the measured changes in potential in either the undoped or the doped specimens. In all three samples, lattice fringe contrast was continuous across the tilt boundaries. High-angle scattering at the position of the boundary in the doped samples would be consistent with an increase in the core in Nb for Ti. However, the EDX data put an upper limit on the change of 1 at.% if it is assumed that the Nb is averaged over a layer of representative width 0.5 nm at the boundary.

APPENDIX

In estimating the errors in the intensity ratios quoted in Table I, it has been assumed that the errors δI_O, δI_{Sr}, and δI_{Ti} in the intensities I_O, I_{Sr}, and I_{Ti} of the counts recorded for each peak are the square root of the number of counts recorded; i.e., it has been assumed that the intensities obey Poisson distributions. Furthermore $I_{Sr} = I_{SrL_\alpha} + I_{SrK_\alpha}$ and $I_{Ti} = I_{TiK_\alpha} + I_{TiK_\beta}$. The error in the counts for niobium has been taken to be the square root of the background intensity at the position of the niobium peak in the spectrum.

The errors in the intensity ratios quoted in Table I have then been calculated for O, Sr, Ti, and Nb from the standard formula whereby if q is a function of several variables $x, \ldots, z$, each of which is measured with small uncertainties $\delta x, \ldots, \delta z$, then the uncertainty δq in q is defined by

$$\delta q = \left[\left(\frac{\partial q}{\partial x} \delta x \right)^2 + \ldots + \left(\frac{\partial q}{\partial z} \delta z \right)^2 \right]^{1/2}$$

for independent random errors.[40] Thus, for example, if $q = I_O/(I_O + I_{Sr} + I_{Ti} + I_{other}) = I_O/I_{total}$, where I_{other} denotes the small sum of counts not attributable to O, Sr, and Ti recorded in the spectrum above the background and where I_{total} is the total number of counts above the background,

$$\delta q = \frac{1}{I_{total}^2} [(I_{Sr} + I_{Ti} + I_{other})^2 \, \delta I_O^2 + I_O^2 (\delta I_{Sr}^2 + \delta I_{Ti}^2)]^{1/2}$$

if it is assumed that δI_{other} is negligible in comparison with δI_O, δI_{Sr}, and δI_{Ti}.

For Nb, where a peak could not be discerned from the background in the EDX spectrum, but where an error δI_{Nb} can be defined, we can choose $q = I_{Nb}/I_{total}$, so that

$$\delta q = \frac{1}{I_{total}^2} [(I_O + I_{Sr} + I_{Ti} + I_{other})^2 \, \delta I_{Nb}^2 + I_{Nb}^2 (\delta I_O^2 + \delta I_{Sr}^2 + \delta I_{Ti}^2)]^{1/2}$$

which for $I_{Nb} \to 0$ becomes simply

$$\delta q = \frac{\delta I_{Nb}}{I_{total}}$$

Thus, for example, for sample M3, spectrum B2, 13 211 counts were recorded at the position of the O peak, together with 42 840 at the positions of the Sr peaks and 24 717 at the position of the Ti peaks. Stripping the background noise from the spectrum gave corrected counts (intensities) for O, Sr, and Ti of $I_O = 12059$, $I_{Sr} = 40396$, and $I_{Ti} = 23377$, together with 448

other counts above the background, giving a total count of $I_{total} = 76280$.

If we take the counts recorded under a peak, including the noise, to estimate δI_O, δI_{Sr}, and δI_{Ti}, then it follows that $\delta I_O = 115$, $\delta I_{Sr} = 207$, and $\delta I_{Ti} = 153$. The background counts at the position of the niobium peak were 1268, so that $\delta I_{Nb} = 36$. Hence it follows that by using the above equations $I_O/I_{total} = 0.1581 \pm 0.0014$, $I_{Sr}/I_{total} = 0.5296 \pm 0.0018$, $I_{Ti}/I_{total} = 0.3065 \pm 0.0017$, and $\delta I_{Nb}/I_{total} = \pm 0.0005$.

References

[1]L. M. Levinson and H. R. Philipp, ''The Physics of Metal Oxide Varistors,'' *J. Appl. Phys.*, **46** [3] 1332–41 (1975).

[2]W. Heywang, ''Resistivity Anomaly in Doped Barium Titanate,'' *J. Am. Ceram. Soc.*, **47** [10] 484–90 (1964).

[3]R. Mauczok and R. Wernicke, ''Ceramic Boundary-Layer Capacitor,'' *Philips Tech. Rev.*, **41** [11/12] 338–46 (1983/84).

[4]J. Maier, G. Schwitzgebel, and H.-J. Hagemann, ''Electrochemical Investigations of Conductivity and Chemical Diffusion in Pure and Doped Cubic $SrTiO_3$ and $BaTiO_3$,'' *J. Solid State Chem.*, **58** [1] 1–13 (1985).

[5]N. Hirose and A. P. West, ''Impedance Spectroscopy of Undoped $BaTiO_3$ Ceramics,'' *J. Am. Ceram. Soc.*, **79** [6] 1633–41 (1996).

[6]Z. Mao and K. M. Knowles, ''Acceptor Segregation to Grain Boundaries in Strontium Titanate Internal Boundary Layer Capacitors,'' *Proc. Electroceram. V*, **2**, 533–36 (1996).

[7]A. Tonomura, ''Electron-Holographic Interference Microscopy,'' *Adv. Phys.*, **41** [1] 59–103 (1992).

[8]F. M. Ross and W. M. Stobbs, ''A Study of the Initial Stages of the Oxidation of Silicon Using the Fresnel Method,'' *Philos. Mag. A*, **63** [1] 1–36 (1991).

[9]F. M. Ross and W. M. Stobbs, ''Computer Modelling for Fresnel Contrast Analysis,'' *Philos. Mag. A*, **63** [1] 37–70 (1991).

[10]V. Ravikumar, R. P. Rodrigues, and V. P. Dravid, ''An Investigation of Acceptor-Doped Grain Boundaries in $SrTiO_3$,'' *J. Phys. D: Appl. Phys.*, **29** [7] 1799–806 (1996).

[11]S. B. Newcomb, C. B. Boothroyd, and W. M. Stobbs, ''Specimen Preparation Methods for the Examination of Surfaces and Interfaces in the Transmission Electron Microscope,'' *J. Microsc.* (*Oxford*), **140** [2] 195–207 (1985).

[12]M. J. Akhtar, Z.-U.-N. Akhtar, R. A. Jackson, and C. R. A. Catlow, ''Computer Simulation Studies of Strontium Titanate,'' *J. Am. Ceram. Soc.*, **78** [2] 421–28 (1995).

[13]H. Yamada and G. R. Miller, ''Point Defects in Reduced Strontium Titanate,'' *J. Solid State Chem.*, **6** [1] 169–77 (1973).

[14]S. B. Desu and D. A. Payne, ''Interfacial Segregation in Perovskites: I, Theory,'' *J. Am. Ceram. Soc.*, **73** [11] 3391–97 (1990).

[15]M. M. McGibbon, N. D. Browning, M. F. Chisholm, A. J. McGibbon, S. J. Pennycook, V. Ravikumar, and V. P. Dravid, ''Direct Determination of Grain Boundary Atomic Structure in $SrTiO_3$,'' *Science*, **266** [Oct. 7] 102–104 (1994).

[16]Y.-M. Chiang and T. Takagi, ''Grain Boundary Chemistry of Barium Titanate and Strontium Titanate: I, High-Temperature Equilibrium Space Charge,'' *J. Am. Ceram. Soc.*, **73** [11] 3278–85 (1990).

[17]Z. Mao and K. M. Knowles, ''Microstructure of Novel Lithium-Doped $SrTiO_3$ Internal Boundary Layer Capacitors,'' *Br. Ceram. Trans.*, **96** [2] 50–56 (1997).

[18]R. E. Dunin-Borkowski, W. O. Saxton, and W. M. Stobbs, ''The Electrostatic Contribution to the Forward-Scattering Potential at a Space Charge Layer in High-Energy Electron Diffraction. I. Theory Neglecting the Effects of Fringing Fields,'' *Acta Crystallogr., A*, **52** [5] 705–11 (1996).

[19]W. H. Press, B. P. Flannery, S. A. Teukolsky, and W. T. Vetterling, *Numerical Recipes*. Cambridge University Press, U.K., 1989.

[20]R. E. Dunin-Borkowski, Z. Mao, C. A. Davis, and K. M. Knowles, in preparation, 1998.

[21]M. O'Keeffe, and J. C. H. Spence, ''On the Average Coulomb Potential (Φ_0) and Constraints on the Electron Density in Crystals,'' *Acta Crystallogr., A*, **50** [1] 33–45 (1994).

[22]G. Pozzi, ''The Influence of the External-Field on Transmission Electron Microscopy Observations of Electric-Fields at Interfaces,'' *J. Phys. D: Appl. Phys.*, **29** [7] 1807–11 (1996).

[23]R. E. Dunin-Borkowski and W. O. Saxton, ''The Electrostatic Contribution to the Forward-Scattering Potential at a Space Charge Layer in High-Energy Electron Diffraction. II. Fringing Fields,'' *Acta Crystallogr., A*, **53** [2] 242–50 (1997).

[24]P. B. Hirsch, A. Howie, R. Nicholson, D. W. Pashley, and M. J. Whelan, *Electron Microscopy of Thin Crystals*, 2nd ed. Robert E. Krieger Publishing Co., Huntington, NY, 1977.

[25]D. Rez, P. Rez, and I. Grant, ''Dirac-Fock Calculations of X-ray Scattering Factors and Contributions to the Mean Inner Potential for Electron Scattering,'' *Acta Crystallogr., A*, **50** [4] 481–97 (1994).

[26]A. R. Preston, Department of Materials Science and Metallurgy, University of Cambridge, Pembroke Street, Cambridge CB2 3QZ, U.K., private communication, 1996.

[27]A. Weickenmeier and H. Kohl, ''Computation of Absorptive Form-Factors for High-Energy Electron-Diffraction,'' *Acta Crystallogr., A*, **47** [9] 590–97 (1991).

[28]F. Kara, R. E. Dunin-Borkowski, C. B. Boothroyd, J. A. Little, and W. M. Stobbs, ''Fresnel Contrast Analysis of Composition Changes and Space Charge at Grain Boundaries in Mullite,'' *Ultramicroscopy*, **66** [1–2] 59–71 (1997).

[29]S. M. Sze, *Physics of Semiconductor Devices*, 2nd ed., p. 77. Wiley, New York, 1981.

[30]S. B. Desu and D. A. Payne, ''Reply to 'Comment on Interfacial Segregation in Perovskites: I–IV','' *J. Am. Ceram. Soc.*, **75** [7] 2020–24 (1992).

[31]K. L. Kliewer and J. S. Koehler, ''Space Charge in Ionic Crystals. I. General Approach with Application to NaCl,'' *Phys. Rev.*, **140** [4A] A1226–A1240 (1965).

[32]J. Frenkel, *Kinetic Theory of Liquids*; pp. 36–41. Dover Publications, New York, 1946.

[33]F. A. Kröger and H. J. Vink, *Solid State Physics*, Vol. 3; p. 307. Edited by F. Seitz and D. Turnbull Academic Press, New York, 1956.

[34]Y.-M. Chiang and T. Takagi, ''Comment on 'Interfacial Segregation in Perovskites: I–IV','' *J. Am. Ceram. Soc.*, **75** [7] 2017–19 (1992).

[35]U. Balachandran and N. G. Eror, ''Electrical Conductivity in Lanthanum-Doped Strontium Titanate,'' *J. Electrochem. Soc.: Solid State Sci. Tech.*, **129** [5] 1021–26 (1982).

[36]J. A. S. Ikeda and Y.-M. Chiang, ''Space Charge Segregation at Grain Boundaries in Titanium Dioxide: I, Relationship between Lattice Defect Chemistry and Space Charge Potential,'' *J. Am. Ceram. Soc.*, **76** [10] 2437–46 (1993).

[37]N.-H. Chan, R. K. Sharma and D. M. Smyth, ''Nonstoichiometry in $SrTiO_3$,'' *J. Electrochem. Soc.: Solid State Sci. Technol.*, **128** [8] 1762–69 (1981).

[38]Y.-M. Chiang and T. Takagi, ''Grain Boundary Chemistry of Barium Titanate and Strontium Titanate: II, Origin of Electrical Barriers in Positive-Temperature-Coefficient Thermistors,'' *J. Am. Ceram. Soc.*, **73** [11] 3286–91 (1990).

[39]G. J. Wood, W. M. Stobbs, and D. J. Smith, ''Methods for the Measurement of Rigid-Body Displacements at Edge-On Boundaries Using High-Resolution Electron Microscopy,'' *Philos. Mag. A*, **50** [3] 375–71 (1984).

[40]J. R. Taylor, *An Introduction to Error Analysis*; p. 73. University Science Books, Mill Valley, CA, 1982. □